JACS
JOURNAL OF THE AMERICAN CHEMICAL SOCIETY
Article
pubs.acs.org/JACS

A High-Spin Iron(IV)−Oxo Complex Supported by a Trigonal Nonheme Pyrrolide Platform

Julian P. Bigi,[†,§] W. Hill Harman,[†,§] Benedikt Lassalle-Kaiser,[⊥] Damon M. Robles,[∥] Troy A. Stich,[∥] Junko Yano,[⊥] R. David Britt,*[,∥] and Christopher J. Chang*[,†,‡,§]

[†]Department of Chemistry and [‡]The Howard Hughes Medical Institute, University of California Berkeley, Berkeley, California 94720, United States

[§]Chemical Sciences Division and [⊥]Physical Biosciences Division, Lawrence Berkeley National Laboratory, Berkeley, California 94720, United States

[∥]Department of Chemistry, University of Califoria, Davis, Davis, California 95616, United States

Ⓢ *Supporting Information*

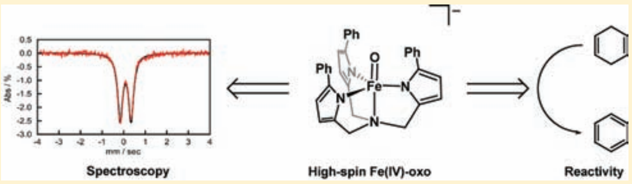

ABSTRACT: We report the generation and characterization of a new high-spin iron(IV)−oxo complex supported by a trigonal nonheme pyrrolide platform. Oxygen-atom transfer to $[(tpa^{Mes})Fe^{II}]^-$ (tpa^{Ar} = tris(5-arylpyrrol-2-ylmethyl)amine) in acetonitrile solution affords the Fe(III)−alkoxide product $[(tpa^{Mes2MesO})Fe^{III}]^-$ resulting from intramolecular C−H oxidation with no observable ferryl intermediates. In contrast, treatment of the phenyl derivative $[(tpa^{Ph})Fe^{II}]^-$ with trimethylamine *N*-oxide in acetonitrile solution produces the iron(IV)−oxo complex $[(tpa^{Ph})Fe^{IV}(O)]^-$ that has been characterized by a suite of techniques, including mass spectrometry as well as UV−vis, FTIR, Mössbauer, XAS, and parallel-mode EPR spectroscopies. Mass spectral, FTIR, and optical absorption studies provide signatures for the iron−oxo chromophore, and Mössbauer and XAS measurements establish the presence of an Fe(IV) center. Moreover, the Fe(IV)−oxo species gives parallel-mode EPR features indicative of a high-spin, $S = 2$ system. Preliminary reactivity studies show that the high-spin ferryl tpa^{Ph} complex is capable of mediating intermolecular C−H oxidation as well as oxygen-atom transfer chemistry.

■ INTRODUCTION

Iron centers supported by heme and nonheme ligands are potent oxidants in natural and synthetic systems.[1] In particular, nonheme iron(IV)−oxo intermediates are implicated in a diverse array of important biological oxidation processes, including hydroxylation, desaturation, ring-closing, and halogenation reaction pathways.[2−7] Interestingly, whereas iron(IV)−oxo species proposed as active oxidants in these aforementioned reactions possess high-spin, $S = 2$ ground states, the vast majority of synthetic iron(IV)−oxo complexes reside in intermediate-spin, $S = 1$ ground states.[8−30] Indeed, synthetic high-spin iron(IV)−oxo complexes remain rare and are limited to seminal contributions by Bakac, Que, and Borovik.[31−34] As such, the identification and characterization of new iron−oxo species, particularly with high-spin ground states, is of fundamental interest in elucidating underlying principles of their reactivity.

To meet this goal, we have initiated a program aimed at studying basic aspects of electronic structure, magnetism, and reactivity at synthetic iron centers,[35−38] with recent efforts focusing on hybrid ligand architectures that combine features of both heme and nonheme systems.[35,37−43] We now report the generation, spectroscopic characterization, and reactivity of a new high-spin iron(IV)−oxo complex supported by a three-fold symmetric pyrrolide platform. A combination of mass spectrometry, UV−vis, FTIR, Mössbauer, XAS, and parallel-mode EPR measurements provides a coherent picture for this rare synthetic, $S = 2$ ferryl system, and preliminary reactivity studies show that this species is capable of intermolecular C−H oxidation and oxygen-atom transfer chemistry.

■ RESULTS AND DISCUSSION

Oxidation of $[(tpa^{Mes})Fe]^-$ Provides the Corresponding Fe^{III}−Alkoxide Complex. Previous work from our laboratory described N_2O activation and intra- and intermolecular C−H oxidation reactivity with iron complexes supported by three-fold symmetric tpa^{Ar} ligands (tpa^{Ar} = tris(5-arylpyrrol-2-ylmethyl)amine) and suggested the involvement of a putative iron(IV)−oxo species.[35] We sought to identify and characterize discrete ferryl intermediates in this platform, and initial experiments centered on oxygen-atom transfer reactions to the mesityl derivative $[(tpa^{Mes})Fe^{II}]^-$ (**1**). In contrast to the intermolecular oxidation reactivity observed in ethereal solvents with relatively weak C−H bonds (THF, DME, etc.) to give the iron(III)−hydroxide complex $[(tpa^{Mes})Fe^{III}(OH)]^-$ (**2**) after oxygen transfer and subsequent hydrogen-atom abstraction

Received: July 27, 2011
Published: January 4, 2012

dx.doi.org/10.1021/ja207048h | *J. Am. Chem.Soc.* 2012, 134, 1536−1542

Scheme 1. Oxygen-Atom Transfer Reactivity and Formation of an Iron(IV)−Oxo Species Supported by Nonheme tpa^{R} Ligands

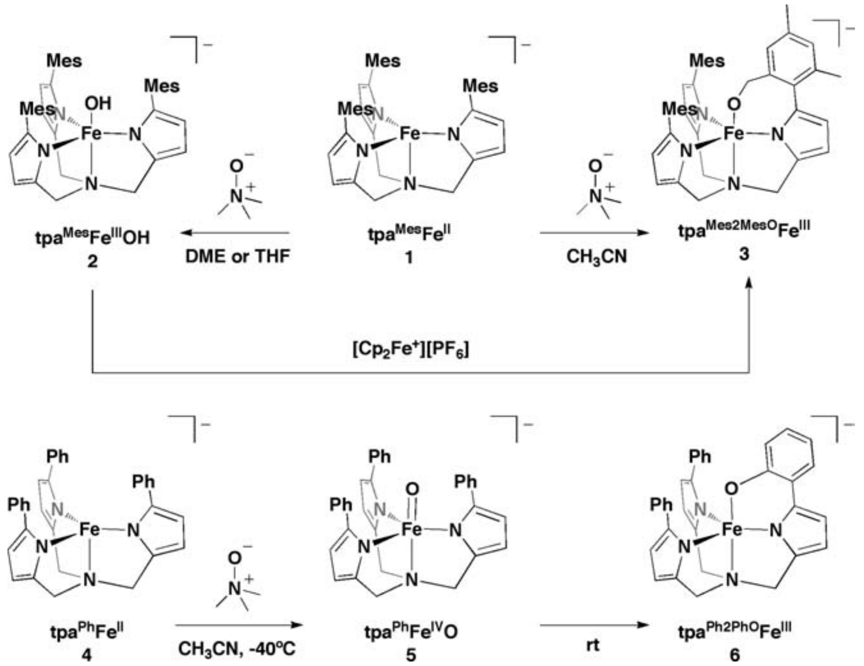

chemistry,[35] treatment of **1** with trimethylamine *N*-oxide in the more oxidatively robust solvent acetonitrile exclusively affords the iron(III)−alkoxide product [(tpa^{Mes2MesO})Fe^{III}]$^-$ (**3**) resulting from intramolecular benzylic C−H oxidation of one of the pendant mesityl arms (Scheme 1 and Figure S1 of Supporting Information [SI]). We identified the iron(III)−alkoxide product by mass spectrometry and the Mössbauer spectrum of a frozen solution of the reaction mixture at 100 K displayed a single iron(III) product with δ = 0.32 mm/s and ΔE_q = 0.88 mm/s (Figure S2, SI). No intermediates were observed in the conversion from **1** to **3** at a variety of different temperatures. Moreover, ^{1}H NMR and LC/MS analysis of the free tpa ligand isolated after demetalation confirmed ligand oxidation and desymmetrization (see SI and Figure S3).

Oxidation of [(tpa^{Mes})FeOH]$^-$ Also Provides the Fe^{III}−Alkoxide Product. Inspired by elegant work from Borovik showing that a hydrogen-bond-stabilized iron(IV)−oxo species could be obtained by oxidation of an iron(III)−hydroxide precursor,[34] we attempted to treat our iron(III)−hydroxide complex **2** with outer-sphere oxidants, as the cyclic voltammogram of this species shows an irreversible electrochemical oxidation process at reasonable potentials (Figure S4 [SI]). However, even at temperatures as low as −60 °C, reactions of **2** with oxidants like ferrocenium hexafluorophosphate produced the same iron(III)−alkoxide **3** directly with no observable Fe(IV) intermediates (Figure S5 [SI], Scheme 1).

Oxidation of [(tpa^{Ph})Fe]$^-$ Yields the Corresponding Fe^{IV}−Oxo Complex. Undeterred, we turned our attention to the related phenyl derivative [(tpa^{Ph})Fe]$^-$ (**4**) to pursue high-valent ferryl species. We reasoned that the aryl C−H bonds on the pendant phenyl groups of this ligand would be comparatively less reactive than their benzylic C−H counterparts on tpa^{Mes} and thus enhance the stability of potential high-valent iron species prone to decomposition by C−H functionalization.[44] Indeed, upon oxidation of **4** with trimethylamine *N*-oxide in acetonitrile solution at −40 °C, we observe the appearance of a new species **5** with a strong absorption band at 400 nm and a weaker absorption feature centered around 900 nm; the latter peak is reminiscent of the near-IR absorptions that are characteristic of synthetic iron(IV)−oxo complexes (Figure 1).[21] Importantly, the conversion of **4** to **5** proceeds with clean isosbestic behavior. The spectrum of **5** remains unchanged for hours when kept at −40 °C and at concentrations near 0.5 mM. However, more concentrated solutions of **5** (~10 mM) decompose with a half-life of approximately one hour, which to date has precluded isolation of solid samples of **5**. Nevertheless, identification of **5** as an iron(IV)−oxo complex comes from electrospray mass spectrometry on a cold acetonitrile solution of this species, where the most prominent signal in the spectrum has an *m/z* value of 551.151 that is consistent with the value expected for the iron(IV)−oxo complex [(tpa^{Ph})Fe(O)]$^-$ (predicted *m/z* = 551.153) (Figures 2 and S6 [SI]). Moreover, within seconds, the most prominent signal shifts to an *m/z* value of 550.147, corresponding to the previously reported iron(III)-phenoxide complex [(tpa^{Ph2PhO})Fe^{III}]$^-$ (**6**) (predicted *m/z* = 550.146) produced from

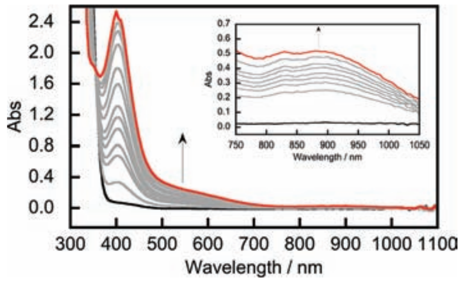

Figure 1. UV/vis spectra monitoring the oxidation of a 0.40 mM solution of **4** in acetonitrile with trimethylamine-*N*-oxide at −40 °C to produce iron(IV)−oxo complex **5**. (Inset) Growth of near-IR band for an analogous experiment run at a higher concentration of **4** (8.0 mM).

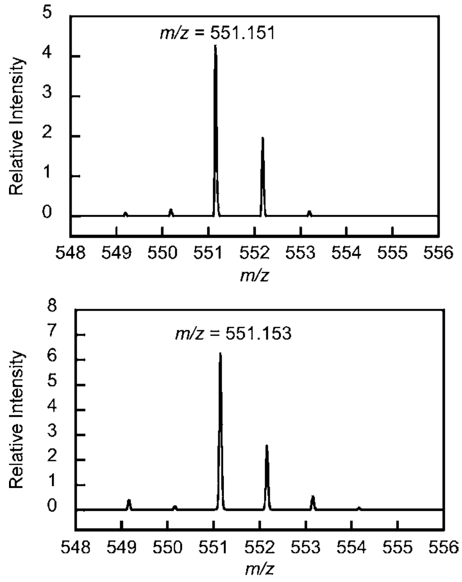

Figure 2. The electrospray ionization mass spectrum of **5**, showing the experimentally observed (top) and theoretical (bottom) isotopic distribution pattern for $[(\mathrm{tpa}^{\mathrm{Ph}})\mathrm{FeO}]^-$.

intramolecular aryl C−H oxidation (Figures S7 and S8 [SI], Scheme 1).

Spectroscopic Characterization of the Fe$^{\mathrm{IV}}$−Oxo Complex: Identifying the Ferryl Chromophore and Fe(IV) Oxidation State. With the aforementioned result in hand, we proceeded to characterize this new iron(IV)−oxo complex using a variety of spectroscopic methods. Our findings from FTIR, Mössbauer, and XAS/EXAFS experiments are summarized as follows.

FTIR Spectroscopy. First, in situ react-IR spectroscopy of **5** generated from reaction of **4** with trimethylamine *N*-oxide in acetonitrile solution at −35 °C showed a new band at 850 cm^{-1}, which shifted to 814 cm^{-1} upon ^{18}O labeling (Figure 3).

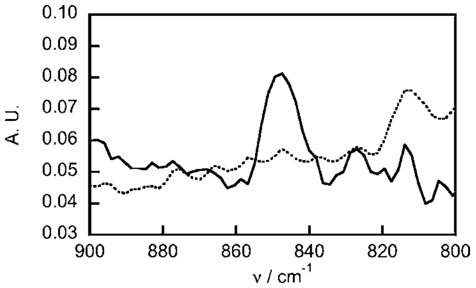

Figure 3. IR spectrum of **5** generated in situ by trimethylamine-*N*-oxide oxidation of **4** in acetonitrile at −35 °C (^{16}O: solid line; ^{18}O: dotted line).

We assign this band to an Fe═O vibration on the basis of agreement with the shift expected for a harmonic Fe−O oscillator model (38 cm^{-1}) and with the values reported for the related TMG$_3$tren and H$_3$buea ferryl systems.[32,34,45]

Mössbauer Spectroscopy. The Mössbauer spectrum of a frozen solution of 5 at 4.2 K showed a single iron-containing product with parameters consistent with iron(IV) with $\delta = 0.09$ mm/s and $\Delta E_q = 0.51$ mm/s (Figure 4). In particular, the near zero isomer shift is characteristic of an Fe(IV) oxidation state and is in close agreement with other ferryl species in the literature.[21,31,32,34]

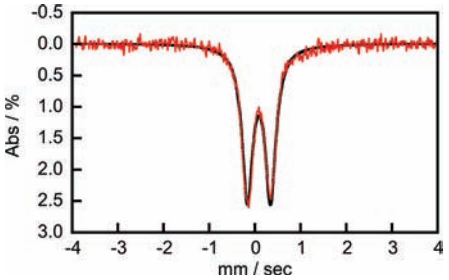

Figure 4. Mössbauer spectrum of a 85 mM frozen solution of **5** in acetonitrile acquired at 4.2 K. A least-squares fit to the data (solid black line) provided the following parameters: $\delta = 0.09$ mm/s, $\Delta E_q = 0.51$ mm/s.

XAS/EXAFS. The Fe K-edge X-ray absorption spectrum of a frozen acetonitrile solution of **5** shows an edge energy of 7122.0 eV (at $F/I_0 = 0.5$), which represents a shift of 3.2 eV as compared to **4** and is consistent with an oxidation of Fe(II) to Fe(IV) (Figure 5 top). The pre-edge region in **4** possesses two features at 7110.9 and 7112.5, with areas of 19.7 and 2.7 units, respectively (Figure S9 and Table S1,SI). Such a pre-edge splitting has been observed previously in the case of iron complexes in C$_{3v}$ geometries[46] and is explained by the noncentrosymmetric nature of the coordination environment as observed in **4**. Upon oxidation to **5**, the pre-edge region shows a strong main feature at 7112.3 eV, which is best fit with two components at 7112.3 and 7114.0 eV, with areas of 28.0 and 4.3 units, respectively (Figure S10 and Table S1, SI). The presence of two peaks in this pre-edge is in agreement with the observations made by England et al. on a $S = 2$ Fe(IV)−oxo complex[32] and is theoretically explained by a splitting of the α and β d_{z^2} orbitals.[47]

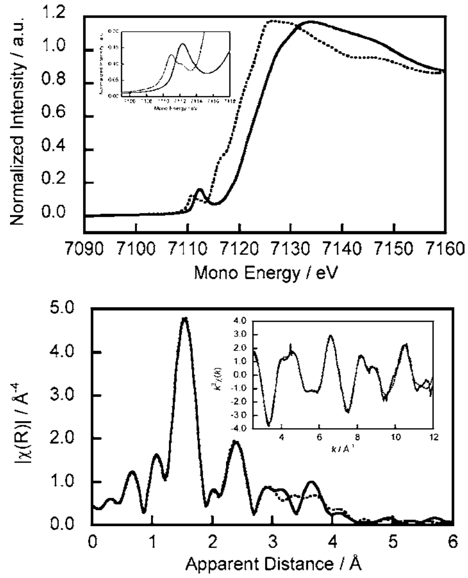

Figure 5. (Top) Fe K-edge XANES and pre-edge (inset) of **4** (dotted trace) and **5** (solid trace). (Bottom) EXAFS Fourier transform and k^3-weighted oscillations (inset) of **5** (solid trace) and the best fit (dotted trace).

The first shell of the EXAFS Fourier transform of **4** was fit with four scatterers at 2.03 Å from the iron(II) center (Table S2, SI), corresponding to an average of the equatorial and axial N ligands. The EXAFS of **5** could be fit with similar parameters, using four paths at 1.99 Å. However, the fit quality was significantly improved (as seen from the decrease in *R* factor and reduced χ^2 values) by adding a Fe−O path at 1.62 Å (Figure 5 bottom and Table S1, SI). The contribution of this Fe−O vector is not seen as a separated peak in the Fourier transform due to its interaction with the four scatterers at 1.99 Å. The 1.62 Å scatterer observed in **5** is attributed to the oxygen of a newly formed Fe−O bond, the distance being in line with that of previously reported $S = 2$ Fe(IV)−oxo compounds.[32−34]

Parallel-Mode EPR Spectroscopy Reveals a High-Spin $S = 2$ Fe^{IV}−Oxo Complex. With information on the iron−oxo chromophore and iron(IV) oxidation state in hand, we proceeded to examine the magnetic properties of this new ferryl species by EPR. Parallel-mode X-band EPR spectra of **5** acquired below 8 K possess almost no intensity (Figure 6). As the temperature increased, however, a broad derivative-shaped feature centered at $g = 8.5$ grows in, which is distinct from spectral features corresponding to either **4** or **6** (cf. Figures S12, S13 [SI] and 6 and 7). Such behavior is consistent with **5** being a $S = 2$ system with a positive axial zero-field splitting constant *D*. The temperature-dependence of the intensity of this derivative feature is best fit using a value of $D = +4.3$ cm^{-1}. The field position of this resonance and the asymmetry of the corresponding line shape are diagnostic of the central value and distribution of the rhombic zero-field splitting term *E*. All EPR spectral features and their corresponding temperature dependence are well-simulated using a $S = 2$ spin system with $g = 2$,$D = +4.3$ cm^{-1}, $E/D = 0.098$ and $\sigma_{E/D} = 0.02$ (Figures 6 and 7). This value of *D* is very similar to that found for other high-spin Fe(IV) oxo species with trigonal bipyramidal ligand sets ($D = 4.0$ cm^{-1} for H$_3$buea;[34] 5.0 cm^{-1} for TMG$_3$tren;[32] and 10.0 cm^{-1} TauD-J).[48] The spectral fit requires a rather large line width (8 mT) and distribution in *E* ($\sigma_{E/D}$, one standard deviation in the *E*/*D* ratio) compared to those determined for Fe(IV)O[H$_3$buea]$^-$.[34] This behavior reflects a distribution in the precise electronic-structure description of **5** that likely results from increased disorder of the phenyl groups on the tpa ligand relative to the urealato groups of [H$_3$buea]$^{3-}$ which can hydrogen bond to the ferryl-oxo.

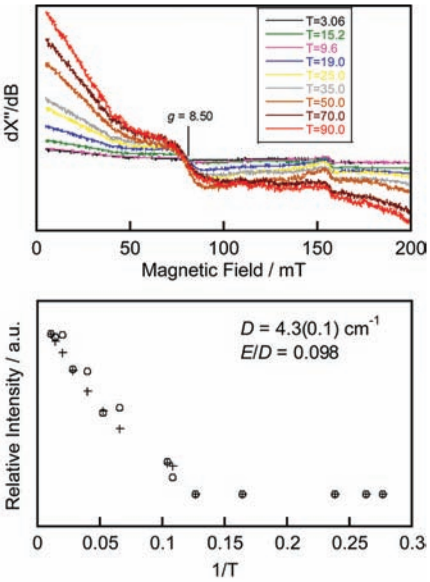

Figure 6. Temperature dependence of parallel-mode EPR spectrum of **5** from 3 to 90 K (top). Relative intensity of $g = 8.50$ feature versus 1/T for experimental (○) and calculated (+) spectra (bottom). Best fit analysis provides a value for the axial zero-field splitting paramater, *D*, of 4.3 cm^{-1}.

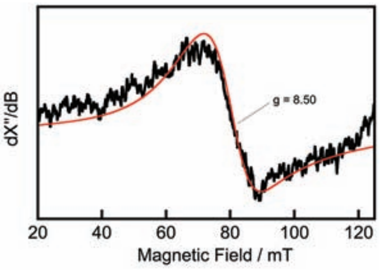

Figure 7. Parallel-mode X-band (9.38 GHz) EPR spectrum of **5** (black) and simulation (red) in 1:1 acetonitrile/toluene. Spectrometer conditions: temperature 40 K, incident power 2.02 mW, modulation amplitude 0.8 mT. Simulation parameters: $D = +4.32$ cm^{-1}, $E/D = 0.098$, $\sigma_{E/D} = 0.02$, and a line broadening of 8 mT.

To further confirm the electronic structure, spectra were calculated for an intermediate, $S = 1$, spin system. However, no single parameter set was found that correctly modeled both the line shape and field position of the observed resonance signal. Furthermore, to the best of our knowledge, there are no examples in the literature of 3d^4 complexes with trigonal bipyramidal ligand field symmetry that have been characterized as $S = 1$ spin systems. A dramatic distortion in the trigonal ligand field would be required to produce this state, one that is not supported by the EXAFS data (vide supra). With the $S = 1$ formulation of **5** ruled out on this basis, and in concert with the combined data from a suite of other spectroscopic measurements we assign **5** as being a high-spin, $S = 2$ iron(IV)−oxo complex.

Preliminary Reactivity Studies Establish that the tpa-Supported Ferryl Can Participate in C−H Abstraction and Oxygen-Atom Transfer Chemistry. Finally, preliminary reactivity studies of high-spin ferryl **5** are consistent with the presence of a reactive yet sterically shielded iron−oxo unit, which is expected for this complex bearing a bulky ancillary ligand. For example, **5** fails to react with oxygen-atom acceptors ranging from cyclooctene to thioanisole to triphenylphosphine. In contrast, **5** reacts rapidly upon mixing with the smaller phosphine PMe$_2$Ph to produce the phosphine oxide in 89% yield (Figure S14, SI). In addition, a 3.0 mM acetonitrile solution of **5** reacts rapidly with 1,4-cyclohexadiene (CHD) to produce benzene (90% yield) with a second-order rate constant of 1.4 M^{-1} s^{-1} at −30 °C, showing that ferryl **5** is capable of intermolecular hydrogen-atom transfer (HAT) chemistry (Figures 8 and S15 [SI]). The steric demands on **5** preclude

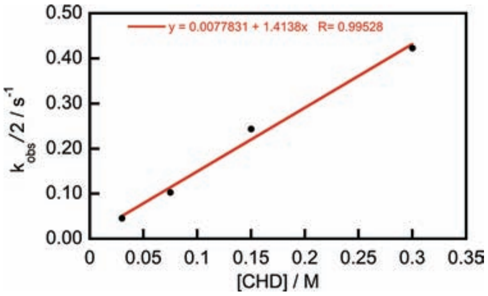

Figure 8. Plot of $k_{obs}/2$ vs [CHD] for the reaction of **5** with CHD at −30 °C. The second-order rate constant is obtained from the slope to be 1.4 M^{-1} s^{-1}.

reactivity with other hydrogen-atom donors such as 9,10-dihydroanthracene (DHA) or xanthene despite their weaker C−H bond strengths compared to those of CHD. As such, current efforts are aimed at reducing the steric crowding at the iron−oxo unit with the hope of increasing reactivity with external substrates.

■ CONCLUDING REMARKS

To close, we have presented the generation of a new high-spin iron(IV)−oxo complex, its characterization by a suite of spectroscopic methods, and its ability to participate in intra- and intermolecular C−H oxidation reactions as well as oxygen-atom transfer to a sterically undemanding phosphine. In particular, Mössbauer and XAS measurements establish the presence of an Fe(IV) center for $[(tpa^{Ph})Fe(O)]^-$, FTIR and UV−vis studies identify the Fe−oxo chromophore, and parallel-mode EPR provides signatures indicative of a high-spin, $S = 2$ system. Taken together, this system adds to the small but growing number of high-spin ferryl complexes in nonheme environments. Ongoing work is geared toward further reactivity studies of high-spin ferryl species in this general manifold, and related group-transfer processes on iron and other first-row transition metals are also under investigation.

■ EXPERIMENTAL SECTION

General Synthetic Details. Unless otherwise noted, all synthetic manipulations were performed under an inert atmosphere of dinitrogen in a Vacuum Atmospheres glovebox or on a vacuum line using standard Schlenk technique. Solvents were dried on a Vacuum Atmospheres Solvent purification system and stored over 3 Å molecular sieves. Acetonitrile was further dried by filtering through a plug of basic alumina immediately prior to use. Molecular sieves, alumina, and Celite were activated by heating at 200 °C under dynamic vacuum for at least 24 h. Potassium hydride was purchased as a suspension in mineral oil, washed with pentane and used as a dry solid in the glovebox. 1,4-Cyclohexadiene was degassed with three freeze−pump−thaw cycles and dried over 3 Å molecular sieves. ^{18}O-labeled trimethylamine-*N*-oxide was prepared according to a literature procedure[49] using ^{18}O-labeled hydrogen peroxide (90% $^{18}O_2$) purchased from Cambridge Isotope Laboratories (Andover, MA). All other reagents were purchased from Sigma-Aldrich and used as received. All glassware was dried by storage in an oven at 170 °C for at least 12 h before use. The iron complexes $[(tpa^{Mes})Fe][K(dme)_2]$ (**1**), $[(tpa^{Mes})FeOH][K(dme)]$ (**2**) and $[(tpa^{Ph})Fe][Na(thf)]$ (**4**) were prepared according to literature procedures.[35]

Synthesis of $[(tpa^{2MesMesO})Fe]K$ (3). An acetonitrile solution of trimethylamine-*N*-oxide (0.018 g, 0.24 mmol) was added to an acetonitrile solution of $[(tpa^{Mes})Fe][K(dme)_2]$ (**1**) (0.047 g, 0.054 mmol) and stirred for 3 h. Over the course of 30 min the colorless solution turned dark brown. The solvent was then removed in vacuo, and the resulting brown solid residue was recrystallized by layering a concentrated THF solution of the product under ether to provide clumps of brown crystals of **3**. ESI MS ($[3\text{-K}]^-$): *m*/*z* calcd for $C_{42}H_{44}FeN_4O$ 676.2870, found at 676.2849. The oxidized ligand was separated from the metal and isolated by filtering an acetonitrile solution of **3** through a plug of silica and removing the solvent in vacuo. LC/MS ($[H_3tpa^{2MesMesO}]^-$): *m*/*z* calcd for $C_{42}H_{47}N_4O$ 623.38, found at 623.4. ^{1}H NMR spectrum (300 MHz, CD_3CN): δ 9.66 (s, 1H), 9.37 (s, 2H), 7.06 (s, 1H), 6.98 (s, 1H), 6.86 (s, 4H), 6.05 (s, 3H), 5.90 (s, 1H), 5.79 (s, 2H), 4.23 (s, 2H), 3.54 (s, 6H), 2.28 (s, 3H), 2.23 (s, 6H), 2.10 (s, 3H), 2.01 (s, 12H) (Figure S3, SI).

Generation of $[(tpa^{Ph})FeO]Na$ (5). An acetonitrile solution of trimethylamine-*N*-oxide (4 equiv) was added to an acetonitrile solution of $[(tpa^{Ph})Fe][Na(thf)]$ (**4**) at −40 °C to produce a dark-red/brown solution which could be monitored by UV/vis for the characteristic near-IR band near 900 nm (∼1−10 mM). The solutions were immediately frozen at 77K for Mössbauer and XAS experiments (∼70−100 mM), and EPR samples were prepared similarly using a 1:1 mixture of toluene and acetonitrile as solvent (∼1−10 mM). Mass spectrometry experiments were performed on thawing acetonitrile solutions (vide infra). ESI MS ($[5\text{-Na}]^-$): *m*/*z* calcd for $C_{33}H_{27}FeN_4O$ 551.153, found at 551.151 (Figure 2).

General Physical Methods. Mass spectrometry measurements were performed on either an LTQ Orbitrap (Thermo Scientific, West Palm Beach, FL) or Waters Q-TOF Premier (Milford, MA) spectrometer at the QB3/Chemistry Mass Spectrometry Facility at UC Berkeley. Elemental analyses were performed on a Perkin-Elmer 2400 Series II combustion analyzer (Waltham, MA) in the Microanalytical Laboratory in the College of Chemistry, University of California, Berkeley, California. Cyclic voltammetry experiments were conducted on a BASi Epsilon potentiostat (West Lafayette, IN) using a glassy carbon disk working electrode, a platinum wire auxiliary, and a platinum wire as a floating reference. Potentials were referenced using either ferrocene or cobaltocene as internal standards. In situ IR spectra were measured on a Mettler-Toledo ReactIR iC10 instrument (Columbus, OH). ^{1}H NMR spectra were recorded on Bruker spectrometers operating at 300 or 400 MHz as noted. Chemical shifts are reported in ppm and referenced to residual protiated solvent, and coupling constants are reported in hertz. UV−vis spectra were acquired on a Varian Cary 50 BIO UV−visible spectrophotometer (Agilent Technologies, Santa Clara, CA) with a Unisoko cryostat attachment for temperature control (Unisoku Co, Osaka, Japan).

Mass Spectrometric Detection of 5. The thermally unstable iron(IV)−oxo complex **5** was analyzed using electrospray ionization in negative V mode on a Waters Q-TOF Premier spectrometer. Samples of **5** were generated at −35 °C as ca. 1 mM acetonitrile solutions, frozen in liquid nitrogen, and introduced into the mass spectrometer as a thawing solution using a syringe pump. ESI source parameters were adjusted as follows: capillary voltage, 0.8 kV; sampling cone voltage, 19 V; source temperature, 60 °C; desolvation temperature, 40 °C.

Mössbauer Spectroscopy. Mössbauer spectra were recorded in constant acceleration mode as frozen acetonitrile solutions (∼80−100 mM) between room temperature and 4.2 K in a Janis Research Co. cryostat (Willmington, MA) and analyzed using the WMOSS software package (See Co, Medina, MN). Isomer shifts are reported relative to α-iron (27 μm foil) at room temperature.

X-ray Absorption Spectroscopy. X-ray data were collected at the Stanford Synchrotron Radiation Lightsource (SSRL) on beamline 7-3 at an electron energy of 3.0 GeV with an average current of 300 mA. The radiation was monochromatized by a Si(220) double-crystal monochromator. The intensity of the incident X-ray was monitored by an N_2-filled ion chamber (I0) in front of the sample. Solution samples were placed in 60-μL plastic sample holders, frozen with liquid nitrogen and collected at 20 K using a helium-cooled cryostat. Data were collected as fluorescence excitation spectra with a Ge 30 element detector (Canberra). Energy was calibrated by the first peak maximum of the first derivative of an iron foil (7111.20 eV). The standard was placed between two N_2-filled ionization chambers (I1 and I2) after the sample. The integrity of the sample upon measurement was assured by the XANES energy shift, and we did not observe any edge shift during the several scans under the current experimental condition.

XAS/EXAFS Data Reduction and Analysis. Pre-edge peaks of **4** and **5** were fit using the EDG_FIT program from the EXAFSPAK suite. (Drs. Graham George and Ingrid Pickering, SSRL) The parameters obtained from the fits are gathered in Table S1 (SI).

Data reduction of the EXAFS spectra was performed using EXAFSPAK. Pre-edge and post-edge backgrounds were subtracted from the XAS spectra, and the results were normalized with respect to edge height. Background removal in *k*-space was achieved through a five-domain cubic spline. Curve fitting was performed with Artemis and IFEFFIT software using ab initio-calculated phases and amplitudes from the program FEFF 8.2.[51,52] These ab initio phases and amplitudes were used in the EXAFS equation:

$$\chi(k) = S_0^2 \sum_j \frac{N_j}{kR_j^2} f_{\mathrm{eff}_j}(\pi, k, R_j)\, \mathrm{e}^{-2\sigma_j^2 k^2} \sin(2kR_j + \varphi_{ij}(k))$$

The neighboring atoms to the central atom(s) are divided into *j* shells, with all atoms with the same atomic number and distance from the central atom grouped into a single shell. Within each shell, the coordination number N_j denotes the number of neighboring atoms in shell j at a distance of R_j from the central atom. $f_{\mathrm{eff}_j}(\pi,k,R_j)$ is the ab initio amplitude function for shell j, and the Debye−Waller term $e^{-2\sigma_j^2k^2}$ accounts for damping due to static and thermal disorder in absorber−backscatterer distances. The mean free path term $e^{-2R_j/\lambda_j(k)}$ reflects losses due to inelastic scattering, where $\lambda_j(k)$ is the electron mean free path. The oscillations in the EXAFS spectrum are reflected in the sinusoidal term, $\sin(2kR_j + f_{ij}(k))$ where $f_{ij}(k)$ is the ab initio phase function for shell j. S_0^2 is an amplitude reduction factor due to shake-up/shake-off processes at the central atom(s). The EXAFS equation was used to fit the experimental data using N, R, and the EXAFS Debye−Waller factor (σ^2) as variable parameters. For the energy (eV) to wave vector (k, $Å^{-1}$) axis conversion, E_0 was defined as 7120 eV and the S_0^2 value was fixed to 0.78. EXAFS curve-fitting procedures and the estimation of the uncertainty in the parameters from the fits are described in detail as follows.

EXAFS Curve Fitting Procedure. The best fit parameters for the Fe EXAFS data are summarized in Table S2, SI. As a goodness-of-fit index, we used the R-factor (the absolute difference between theory and data), which is defined as the sum of the squares of the differences between each experimental point and the fit normalized to the sum of the squares of the experimental points.[53] In all fits unless specified, N values were set, while R and σ^2 values were left floating.

We first carried out a fit for **4**, using the parameters obtained from the crystal structure. The EXAFS data are in good agreement with the XRD values. The Fe−N shell at 2.04 Å reflects an average of three equatorial (2.00 Å) and one axial (2.17 Å) N atoms. The Fe−C_1 shell at 2.91 Å reflects an average of the Fe to methylene carbon (2.92 Å) and Fe to pyrrolide proximal carbon (2.85 Å) distances. The Fe−C_2 shell at 3.20 Å reflects a Fe to pyrrolide distal carbon (3.29 Å) pathway with multiple scattering. The Fe−C_3 shell at 4.26 Å corresponds to the distance from Fe to the pyrrolide carbon 4.23 Å away from the Fe center. The 4.26 Å feature arising from the distal pyrrolide ring was absent in the EXAFS spectrum of the $S = 2$ Fe(IV)−O compound reported by England et al.[32]

For **5**, the data was at first fit using the same parameters as **4** (Fit #1). A slight contraction of the Fe−N shell to 1.99 Å and the Fe−C_2 shell to 3.02 Å is observed, which is consistent with an oxidation of the iron center. However, by introducing a short Fe−O shell at 1.62 Å, the fit quality improved significantly, as is shown by the decrease of the R-factor and reduced χ^2 values (Fit #2). The Fe−O vector does not appear as a separate peak in the Fourier transform due to its interaction with the Fe−N shell.

EPR Spectroscopy. All continuous-wave parallel-mode ($B_0 \parallel B_1$) X-band (9.38 GHz) EPR spectroscopic characterization was performed at the CalEPR facility at UC Davis using a Bruker ECS 106 spectrometer (Billerica, MA) equipped with an Oxford Instruments ESR900 liquid helium cryostat and a Bruker TE_{102}/TE_{012} dual-mode cavity (ER4116DM). Temperature control was achieved using an Oxford ITC 403 temperature controller. Spectra were collected under slow passage and nonsaturating conditions. For all presented data, a corresponding spectrum of the solvent (1:1 acetonitrile/toluene) was subtracted to remove signals from baseline artifacts and paramagnetic contaminants present in the cavity. All spectral simulations were carried out using the EasySpin[50] toolbox for MatLab R2010a (MathWorks, Inc., Natwick, MA).

Parallel-Mode EPR Experiments. At 3 K there is essentially no spectral intensity. Signals grow in with increasing temperature that are indicative of a high-spin ($S = 2$) species with a positive axial zero-field splitting constant D (Figure 6). At 40 K, a broad derivative-shaped feature is present at $g = 8.5$ and is assigned to the transition between the levels of the $m_S = \pm 2$ doublet (Figure 7). A best-fit analysis of the temperature dependence of the intensity of this derivative feature allows for the determination of the magnitude of D. Predicted intensities are computed in the following manner. The energy levels for the system are calculated and then populated according to Boltzmann statistics for a particular temperature. The predicted spectrum is then computed as a function of these populations and doubly integrated to give the total spectral intensity. This is then compared to the experimentally determined spectral intensity. The resonant field position of the derivative feature allows for the determination of the central value in the distribution of E/D. All spectral features and their corresponding temperature dependence are well simulated using a $S = 2$ spin system with $g = 2$, $D = +4.3(\pm 0.1)\ \mathrm{cm}^{-1}$, $E/D = 0.098$ and $\sigma_{E/D} = 0.02$ The 40 K perpendicular-mode spectrum of this sample, shows an intense derivative-shaped feature at $g = 4.3$ that is assigned to the Fe(III)-phenoxy product (Figure S13, SI). A small portion of this signal bleeds through to the parallel-mode spectrum due to small misalignments of the B_0 relative to B_1. Notably, the parallel-mode EPR signals described above are distinct from those of the Fe(II) starting complex ($S = 2$), which shows a strong negative feature at $g = 9.50$ (Figure S12, SI).

Phosphine-Oxide Yield from the Reaction of 5 with Me_2PPh. The reaction of **5** with an excess of Me_2PPh was performed in an NMR tube and the yield of $Me_2P(O)Ph$ calculated by integration of the ^{31}P NMR resonances relative to PPh_3 as an internal standard. See Figure S14 in SI for the spectrum.

Benzene Yield from the Reaction of 5 with 1,4-Cyclohexadiene (CHD). The reaction of **5** with an excess of CHD was performed in an NMR tube and the yield of benzene calculated by integration of the ^1H NMR resonances relative to 1,2,4,5-tetramethylbenzene as an internal standard. See Figure S15 in SI for the spectrum.

Kinetics Studies of Reaction of 5 with 1,4-Cyclohexadiene (CHD). A 3.0 mM acetonitrile solution of **4** was prepared in a cuvette in an inert atmosphere glovebox and cooled to −30 °C in the UV/vis spectrophotometer cryostat. An acetonitrile solution of trimethylamine-*N*-oxide was then added via syringe (four equivalents in ca. 0.1 mL) and the formation of **5** was monitored at 900 nm. Once the absorbance of **5** at 900 nm reached a steady value, a precooled (−30 °C) acetonitrile solution of 10−100 equiv of CHD was added via syringe, and the decay of **5** was monitored at 900 nm holding the temperature at −30 °C. The resulting decay curves were fit to a single exponential, allowing extraction of observed rate constants. The observed rate constants were then divided by two to account for the stoichiometry of the reaction and plotted against the concentration of CHD; the slope of the resulting line is the second-order rate constant (Figure 8).

■ ASSOCIATED CONTENT

Ⓢ Supporting Information

Supplementary figures. This material is available free of charge via the Internet at http://pubs.acs.org.

■ AUTHOR INFORMATION

Corresponding Author

chrischang@berkeley.edu; rdbritt@ucdavis.edu

■ ACKNOWLEDGMENTS

This research was supported by DOE/LBNL (403801) to C.J.C., DOE (DE-AC02-05CH11231) to J.Y., and DOE (DE-FG02-10ER16150) to R.D.B. C.J.C. is an investigator with the Howard Hughes Medical Institute. J.P.B. thanks the National Science Foundation for a graduate fellowship. D.M.R. thanks the Alfred P. Sloan Foundation for support. We also thank Rupal Gupta (Carnegie Mellon University) and Stefan Stoll (University of California-Davis) for helpful discussions. Synchrotron facilities were provided by the Stanford Synchrotron Radiation Lightsource (SSRL) operated by DOE OBES. The SSRL Biomedical Technology program is supported by NIH, the National Center for Research Resources, and the DOE Office of Biological and Environmental Research.

■ REFERENCES

(1) Groves, J. T. *J. Inorg. Biochem.* **2006**, *100*, 434−447.
(2) Feig, A. L.; Lippard, S. J. *Chem. Rev.* **1994**, *94*, 759−805.

(3) Que, L. Jr.; Ho, R. Y. N. *Chem. Rev.* **1996**, *96*, 2607−2624.

(4) Baik, M.-H.; Newcomb, M.; Friesner, R. A.; Lippard, S. J. *Chem. Rev.* **2003**, *103*, 2385−2420.

(5) Costas, M.; Mehn, M. P.; Jensen, M. P.; Que, L. Jr. *Chem. Rev.* **2004**, *104*, 939−986.

(6) Vaillancourt, F. H.; Yeh, E.; Vosburg, D. A.; Garneau-Tsodikova, S.; Walsh, C. T. *Chem. Rev.* **2006**, *106*, 3364−3378.

(7) Krebs, C.; Galonic Fujimori, D.; Walsh, C. T.; Bollinger, J. M. *Acc. Chem. Res.* **2007**, *40*, 484−492.

(8) Que, L. Jr.; Dong, Y. *Acc. Chem. Res.* **1996**, *29*, 190−196.

(9) Grapperhaus, C. A.; Mienert, B.; Bill, E.; Weyhermueller, T.; Wieghardt, K. *Inorg. Chem.* **2000**, *39*, 5306−5317.

(10) MacBeth, C. E.; Golombek, A. P.; Young, V. G.; Yang, C.; Kuczera, K.; Hendrich, M. P.; Borovik, A. S. *Science* **2000**, *289*, 938−941.

(11) Lim, M. H.; Rohde, J.-U.; Stubna, A.; Bukowski, M. R.; Costas, M.; Ho, R. Y. N.; Münck, E.; Nam, W.; Que, L. Jr. *Proc. Natl. Acad. Sci. U.S.A.* **2003**, *100*, 3665−3670.

(12) Rohde, J.-U.; In, J.-H.; Lim, M. H.; Brennessel, W. W.; Bukowski, M. R.; Stubna, A.; Münck, E.; Nam, W.; Que, L. Jr. *Science* **2003**, *299*, 1037−1039.

(13) Klinker, E. J.; Kaizer, J.; Brennessel, W. W.; Woodrum, N. L.; Cramer, C. J.; Que, L. Jr. *Angew. Chem., Int. Ed.* **2005**, *44*, 3690−3694.

(14) Martinho, M.; Banse, F.; Bartoli, J.-F.; Mattioli, T. A.; Battioni, P.; Horner, O.; Bourcier, S.; Girerd, J.-J. *Inorg. Chem.* **2005**, *44*, 9592−9596.

(15) Bautz, J.; Bukowski, M. R.; Kerscher, M.; Stubna, A.; Comba, P.; Lienke, A.; Münck, E.; Que, L. Jr. *Angew. Chem., Int. Ed.* **2006**, *45*, 5681−5684.

(16) Goldsmith, C. R.; Stack, T. D. P. *Inorg. Chem.* **2006**, *45*, 6048−6055.

(17) Tiago de Oliveira, F.; Chanda, A.; Banerjee, D.; Shan, X.; Mondal, S.; Que, L. Jr.; Bominaar, E. L.; Münck, E.; Collins, T. J. *Science* **2007**, *315*, 835−838.

(18) Ekkati, A. R.; Kodanko, J. J. *J. Am. Chem. Soc.* **2007**, *129*, 12390−12391.

(19) Korendovych, I. V.; Kryatov, S. V.; Rybak-Akimova, E. V. *Acc. Chem. Res.* **2007**, *40*, 510−521.

(20) Nam, W. *Acc. Chem. Res.* **2007**, *40*, 522−531.

(21) Que, L. Jr. *Acc. Chem. Res.* **2007**, *40*, 493−500.

(22) Chanda, A.; Shan, X.; Chakrabarti, M.; Ellis, W. C.; Popescu, D. L.; Tiago de Oliveira, F.; Wang, D.; Que, L. Jr.; Collins, T. J.; Münck, E.; Bominaar, E. L. *Inorg. Chem.* **2008**, *47*, 3669−3678.

(23) Ray, K.; England, J.; Fiedler, A. T.; Martinho, M.; Münck, E.; Que, L. Jr. *Angew. Chem., Int. Ed.* **2008**, *47*, 8068−8071.

(24) Thibon, A.; England, J.; Martinho, M.; Young, V. G.; Frisch, J. R.; Guillot, R.; Girerd, J.-J.; Münck, E.; Que, L. Jr.; Banse, F. *Angew. Chem., Int. Ed.* **2008**, *47*, 7064−7067.

(25) Abouelatta, A. I.; Campanali, A. A.; Ekkati, A. R.; Shamoun, M.; Kalapugama, S.; Kodanko, J. J. *Inorg. Chem.* **2009**, *48*, 7729−7739.

(26) McGown, A. J.; Kerber, W. D.; Fujii, H.; Goldberg, D. P. *J. Am. Chem. Soc.* **2009**, *131*, 8040−8048.

(27) Mukherjee, A.; Martinho, M.; Bominaar, E. L.; Münck, E.; Que, L. Jr. *Angew. Chem., Int. Ed.* **2009**, *48*, 1780−1783.

(28) Kotani, H.; Suenobu, T.; Lee, Y.-M.; Nam, W.; Fukuzumi, S. *J. Am. Chem. Soc.* **2011**, *133*, 3249−3251.

(29) Morimoto, Y.; Kotani, H.; Park, J.; Lee, Y.-M.; Nam, W.; Fukuzumi, S. *J. Am. Chem. Soc.* **2011**, *133*, 403−405.

(30) Seo, M. S.; Kim, N. H.; Cho, K.-B.; So, J. E.; Park, S. K.; Clemancey, M.; Garcia-Serres, R.; Latour, J.-M.; Shaik, S.; Nam, W. *Chem. Sci* **2011**, *2*, 1039−1045.

(31) Pestovsky, O.; Stoian, S.; Bominaar, E. L.; Shan, X.; Münck, E.; Que, L. Jr.; Bakac, A. *Angew. Chem., Int. Ed.* **2005**, *44*, 6871−6874.

(32) England, J.; Martinho, M.; Farquhar, E. R.; Frisch, J. R.; Bominaar, E. L.; Münck, E.; Que, L. Jr. *Angew. Chem., Int. Ed.* **2009**, *48*, 3622−3626.

(33) England, J.; Guo, Y.; Farquhar, E. R.; Young, V. G. Jr.; Münck, E.; Que, L. Jr. *J. Am. Chem. Soc.* **2010**, *132*, 8635−8644.

(34) Lacy, D. C.; Gupta, R.; Stone, K. L.; Greaves, J.; Ziller, J. W.; Hendrich, M. P.; Borovik, A. S. *J. Am. Chem. Soc.* **2010**, *132*, 12188−12190.

(35) Harman, W. H.; Chang, C. J. *J. Am. Chem. Soc.* **2007**, *129*, 15128−15129.

(36) Soo, H. S.; Komor, A. C.; Iavarone, A. T.; Chang, C. J. *Inorg. Chem.* **2009**, *48*, 10024−10035.

(37) Freedman, D. E.; Harman, W. H.; Harris, T. D.; Long, G. J.; Chang, C. J.; Long, J. R. *J. Am. Chem. Soc.* **2010**, *132*, 1224−1225.

(38) Harman, W. H.; Harris, T. D.; Freedman, D. E.; Fong, H.; Chang, A.; Rinehart, J. D.; Ozarowski, A.; Sougrati, M. T.; Grandjean, F.; Long, G. J.; Long, J. R.; Chang, C. J. *J. Am. Chem. Soc.* **2010**, *132*, 18115−18126.

(39) Shi, Y.; Cao, C.; Odom, A. L. *Inorg. Chem.* **2004**, *43*, 275−281.

(40) King, E. R.; Betley, T. A. *Inorg. Chem.* **2009**, *48*, 2361−2363.

(41) Sazama, G. T.; Betley, T. A. *Inorg. Chem.* **2010**, *49*, 2512−2524.

(42) King, E. R.; Hennessy, E. T.; Betley, T. A. *J. Am. Chem. Soc.* **2011**, *133*, 4917−4923.

(43) Piro, N. A.; Lichterman, M. F.; Harman, W. H.; Chang, C. J. *J. Am. Chem. Soc.* **2011**, *133*, 2108−2111.

(44) Two examples of high-valent iron oxidants stabilized by ligands with phenyl groups: (a) Lange, S. J.; Miyake, H.; Que, L. Jr. *J. Am. Chem. Soc.* **1999**, *121*, 6330−6331. (b) Mukherjee, A.; Martinho, M.; Bominaar, E. L; Münck, E.; Que, L. Jr. *Angew. Chem., Int. Ed.* **2009**, *48*, 1780−1783.

(45) The first example of using resonance Raman to identify the Fe=O stretching frequency in synthetic iron(IV)−oxo complexes: Sastri, C. V.; Park, M. J.; Ohta, T.; Jackson, T. A.; Stubna, A.; Seo, M. S.; Lee, J.; Kim, J.; Kitagawa, T.; Münck, E.; Que, L. Jr.; Nam, W. *J. Am. Chem. Soc.* **2005**, *127*, 12494−12495.

(46) Westre, T. E.; Kennepohl, P.; DeWitt, J. G.; Hedman, B.; Hodgson, K. O.; Solomon, E. I. *J. Am. Chem. Soc.* **1997**, *119*, 6297−6314.

(47) Berry, J. F.; DeBeer George, S.; Neese, F. *Phys. Chem. Chem. Phys.* **2008**, *10*, 4361−4374.

(48) Krebs, C.; Price, J. C.; Baldwin, J.; Saleh, L.; Green, M. T.; Bollinger, J. M. *Inorg. Chem.* **2005**, *44*, 742−757.

(49) Hickinbottom, W. J. *Reactions of Organic Compounds*; Longmans, Green and Co.: New York, 1957; p 420.

(50) Stoll, S.; Schweiger, A. *J. Magn. Reson.* **2006**, *178*, 42−55.

(51) Newville, M. *Synchrotron Rad.* **2001**, *8*, 322−324.

(52) Rehr, J. J.; Albers, R. C. *Rev. Mod. Phys.* **2000**, *72*, 621−654.

(53) Newville, M.; Ravel, B.; Haskel, D.; Rehr, J. J.; Stern, E. A.; Yacoby, Y. *Physica B* **1995**, *208*, 154.